Ionic diffusion in quartz studied by transport measurements, SIMS and atomistic simulations

Ionic diffusion in quartz studied by transport measurements, SIMS and atomistic simulations

Asel Sartbaeva[1]**, Stephen A Wells**[2]**, Simon A T Redfern**[1]**, Richard W Hinton**[3] **and Stephen J B Reed**[1]

[1] Department of Earth Sciences, Downing Street, Cambridge CB2 3EQ, UK
[2] Royal Institution, Albemarle Street, London W1S 4BS, UK
[3] Ion Microprobe Unit, School of Geosciences, Grant Institute (Earth Sciences),
University of Edinburgh, Kings Buildings, West Mains Road, Edinburgh EH9 3JW, UK

E-mail: asar01@esc.cam.ac.uk

Abstract

Ionic diffusion in the quartz–β-eucryptite system is studied by DC transport measurements, SIMS and atomistic simulations. Transport data show a large transient increase in ionic current at the α–β phase transition of quartz (the Hedvall effect). The SIMS data indicate two diffusion processes, one involving rapid Li$^+$ motion and the other involving penetration of Al and Li atoms into quartz at the phase transition. Atomistic simulations explain why the fine microstructure of twin domain walls in quartz near the transition does not hinder Li$^+$ diffusion.

(Some figures in this article are in colour only in the electronic version)

1. Introduction

Microstructure in crystals can have a dramatic effect on chemical transport. It has been shown that chemical transport of Na$^+$ in WO$_3$ is significantly faster in domain walls than in the bulk [1, 2]. However, the effect of twin boundaries is not always to enhance transport. Calleja *et al* [3] simulated the transport of Na$^+$ and Li$^+$ through a quartz crystal with (100) Dauphiné twinning using molecular dynamics. These results showed that twinning reduced the transport rate of Na$^+$ along the twin wall in the [001] direction. This is related to the local structure of quartz at the twin boundary, as the channels are elliptically distorted in the twin wall compared to the bulk material.

The Hedvall effect, an increase of reactivity/diffusivity at the phase transition, is observed in a wide variety of materials [4, 5]. Hedvall showed that with increasing temperature, the reactions of NiO and Co$_3$O$_4$ with silica start at the quartz α–β phase transition, and increase again at the quartz–cristobalite transition.

The question of ionic transport in quartz at the α–β phase transition is therefore interesting. On the one hand the Hedvall effect should give an increase in transport; on the other hand, a fine microstructure of domain walls appears in the incommensurate phase of quartz [6–8] near T_c, and the results of Calleja *et al* [3] suggest that this should hinder transport.

We have studied ionic motion in quartz using β-eucryptite (LiAlSiO$_4$) [9–11] as a source of lithium. In this paper we discuss results from DC transport measurements and SIMS analysis. A dielectric study on Li$^+$ motion in quartz has already been published [12]. Classical simulations were also carried out to investigate the structure of domain walls in quartz. Simulations were performed using the fast framework simulation program GASP [13, 12, 14] and the lattice energy program GULP [15].

2. Experimental details

2.1. Sample preparation

β-eucryptite synthesis and sample preparation are described elsewhere [9–11]. ^{6}Li (Euroso-Top 94.99%) carbonate was used for the synthesis. Quartz samples were cut from natural single crystal perpendicular to the c-axis. The dimensions of the samples were approximately 10 mm $\times$ 10 mm $\times$ 0.8 mm. Couples of β-eucryptite and quartz were used for doping and for transport measurements.

Quartz samples for SIMS labelled as '500', '574' and '610' were doped with ^{6}Li from β-eucryptite at 773, 846 and 883 K respectively for 50 h each. The electric field used for doping was 1600 V cm^{-1}. Sample 'q002' was doped with ^{6}Li during 16 runs: 8 heating (770–900 K) and 8 cooling (900–770 K). Each run was about 20 h. The electric field used was 1800 V cm^{-1}. For ion microprobe analysis all four samples were cut parallel to the c-axis, and mounted in epoxy. The imaging surface was then polished and coated with Au.

2.2. Transport measurements

For the transport measurements [16] the equipment consisted of a DC power-supply, a horizontal furnace, a multi-channel digital data logger and a computer. The heating and cooling was in steps of 1 K with 10 min equilibrating time after each temperature change. The temperature stability of the furnace was approximately $\pm$0.5 K. The samples were mounted between two Pt electrodes using Ag paste for better contacts. The difference between furnace temperature and thermocouple temperature varied from 30 K for low temperature regimes to about 50 K for high temperature regimes. The distance between the thermocouple and the samples was about 2 mm. The temperature calibration on the furnace showed a close to linear offset of the temperature of the thermocouple from the furnace temperature. Using the temperature calibration on the thermocouple all the temperatures were recalculated and the absolute error is $\pm$2 K.

An 1800 V cm^{-1} DC electric potential was used to drive ^{6}Li$^+$ from β-eucryptite into quartz. A multi-channel data logger was used to collect DC current, thermocouple temperature and DC voltage simultaneously. Data were collected at 1 s intervals.

2.2.1. Transport data. Current versus time for heating is shown in figure 1. A transient increase in current occurs at the α–β phase transition at 847 K. After the increase, the current gradually relaxes with time (over about 2–5 min) to almost the previous value.

Figure 2 shows current versus time on cooling. As on heating, there is a transient increase in current, which occurs about 2 K $\pm$ 1 K lower than in the heating runs. Just before the
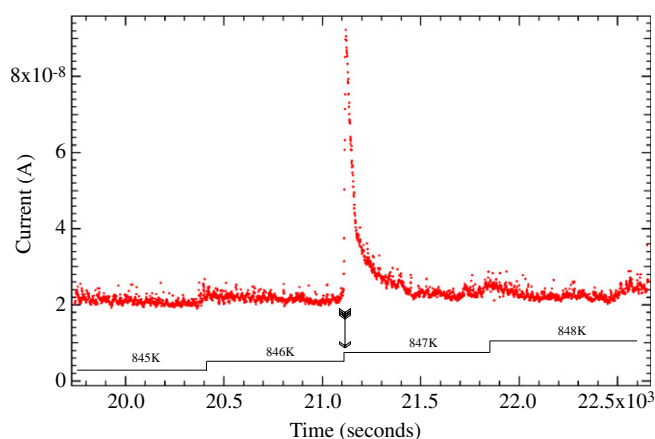
Figure 1. Averaged current versus time during the heating run. Dots are data. The temperature in K is represented schematically. An increase in current corresponds to the temperature change between 846 and 847 K and is indicated by an arrow. The time between each temperature change is 10 min. The data were collected every 1 s.
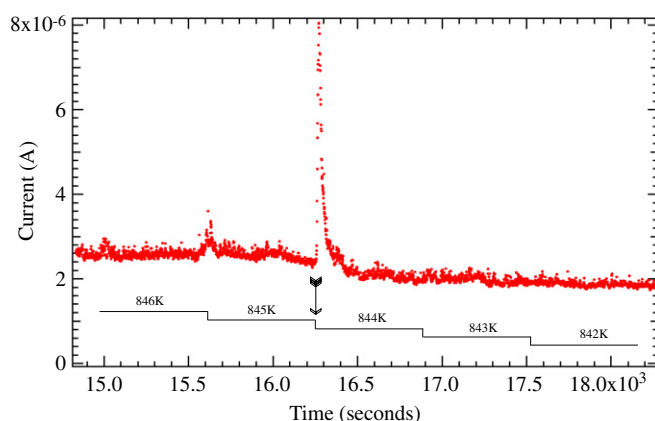

Figure 2. Averaged current versus time during the cooling run. Dots are data. The temperature in K is represented schematically. An increase in current corresponds to the temperature change between 845 and 844 K and is indicated by the arrow.

temperature change from 846 to 845 K there is a smaller peak in current. It was not always reproducible, as it originates from furnace undershoot during the cooling runs. This behaviour was only seen during the some of the cooling runs, thus it was not considered as universal.

The resistance of the quartz sample can be estimated by assuming that β-eucryptite and quartz are in series:

$$R_{\text{quartz}} = R_{\text{total}} - R_{\text{eucryptite}} \tag{1}$$

where R_{quartz} is the resistance of the quartz sample, $R_{\text{eucryptite}}$ is the resistance of the β-eucryptite sample and R_{total} is the resistance of the couple. We have used the value $\sigma = 0.1\ \Omega^{-1}\ \text{mm}^{-1}$ for β-eucryptite from [10]. Figure 3 shows the quartz resistance versus time. At the phase transition, there is a considerable transient decrease of resistance.

The hysteresis in the transition temperature for quartz was expected in the light of quartz 'global' hysteresis studies [6, 7]. However, the dramatic increase of current at the phase
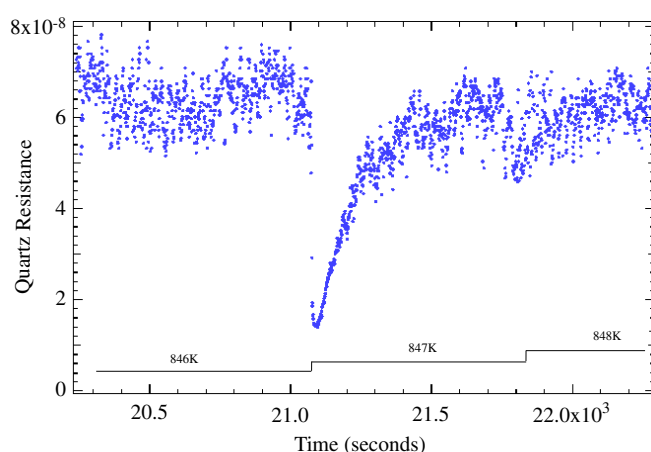
Figure 3. Resistance of quartz in Ω versus time. The temperature in K is represented schematically.

transition was very unexpected. This observation highlights the effect of the structural phase transition on the ionic transport in quartz (the Hedvall effect [4, 5]). However, as SIMS data (section 2.4) will show, the effect occurs not because of Li$^+$ ion motion only, but rather coupled Al + Li motion at the phase transition, thus showing much more complex diffusion behaviour.

2.3. SIMS measurements

The measurements were carried out with a Cameca IMS4f instrument, in the Edinburgh Ion Microprobe Facility. Positive secondary ions were generated by a focused primary beam of ^{16}O$^-$ ions with 15 keV impact energy. Line profiles and images were made using a 0.022 nA beam focused to a spot of about 1 μm. The line profiles were made by moving the sample in 1 μm steps beneath a static primary beam. The area (approximately 50 μm × 30 μm) of the line analysis was presputtered for 5 min using an elongated 11 nA primary beam. An offset of -5 V was used after presputtering to compensate the sample charging.

The images were made using a 1 μm primary beam rastered over an area of 50 μm × 50 μm. The area to be imaged was cleaned by presputtering using a 100 nA primary beam (again rastered over about 50 μm × 50 μm). All images covered the interface region and the edge of the sample.

The spot analyses were made using an 11 nA primary beam focused to a spot of 10–20 μm. A field aperture was used to restrict the area analysed to only 8 μm. Energy filtering was employed to improve the precision of the abundance measurement, only ions between 55 and 95 eV being recorded. Analyses were done on H, ^{6}Li, ^{7}Li, Na, Al and Si. The concentration of H dropped to less then 0.5 ppm during all the runs.

Repeat measurements were performed during short time intervals without changing sample or readjusting any instrumental parameters between different measurements, to reduce the statistical error of the analysis.

2.4. SIMS data

The scans for each element were taken from all the samples near the edge. Repeated measurements were taken on all samples, from 5 to 10 scans on each sample. The beam size
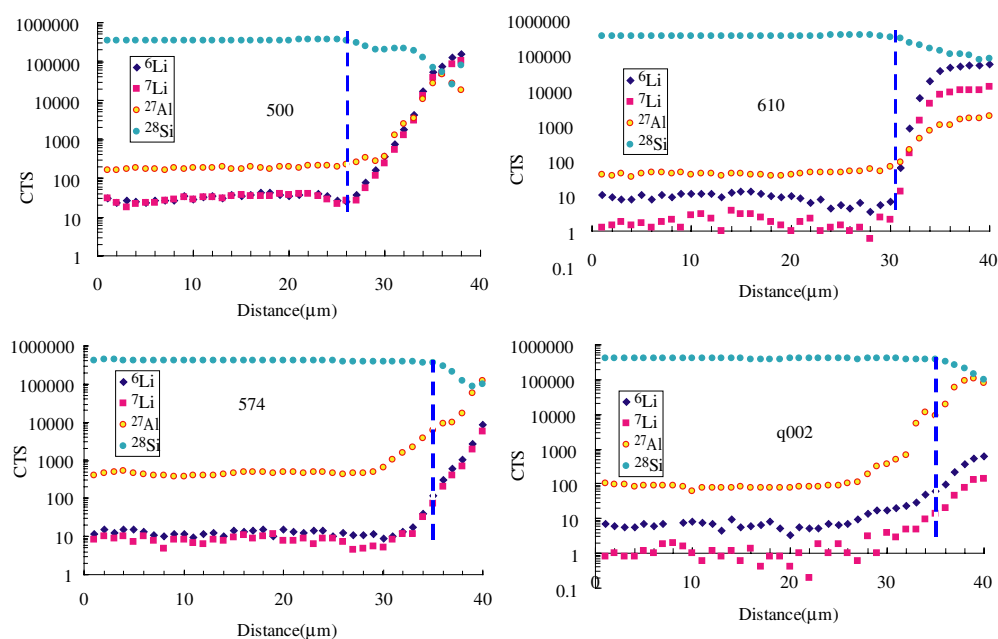
Figure 4. Scans for ^{6}Li, ^{7}Li, ^{27}Al and ^{28}Si from samples '500', '574', '610' and 'q002'. The vertical dashed line shows the edge of the crystal.

was 1 μm, allowing precise observation of the profile. All the scans were about 30–40 μm long.

Figure 4 shows scans of ^{6}Li, ^{7}Li, ^{27}Al and ^{28}Si from samples '500', '574', '610' and 'q002'. Surface contamination was removed by presputtering. First, in the '574' and 'q002' samples a correlated increase in Al and Li concentration near the edge, over a short range of $\simeq 5$ μm, is clearly visible. There is no such increase near the edge for the '500' and '610' samples. Further from the edge there are constant Al and Li concentrations for all four samples. Second, the ^{6}Li to ^{7}Li ratio changes from one sample to another. For '500' this ratio is almost 1:1. It increases slightly for '574', while for '610' and 'q002' it is almost 2:1. The natural abundance of ^{6}Li is 7.59%; therefore the high concentration of ^{6}Li can be attributed to ^{6}Li diffusion throughout the sample from the ^{6}Li-enriched β-eucryptite.

Spot analyses were done in order to find if the concentration of ^{6}Li near the doping edge is different from that in the middle of the crystal. For this a large area was presputtered for 5–10 min and then concentrations of ^{6}Li, ^{7}Li, ^{27}Al and ^{28}Si were collected. The analyses are summarized in table 1. The data which are labelled 'middle' were collected in the middle of the sample area, far away from the doping edge.

As can be seen from table 1, there is an elevated concentration of ^{6}Li in all of the samples, exceeding the concentration of ^{7}Li. While the concentrations of ^{6}Li and ^{27}Al for '500' and '610' samples are relatively low (0.8–1.4 ppm/Si and 17–23 ppm/Si respectively), the concentrations for '574' and 'q002' samples are considerably higher.

Imaging was done on ^{6}Li, ^{7}Li, ^{23}Na, ^{27}Al and ^{28}Si on all four samples. The images were made with a beam size of 1 μm rastered over an area of 50 μm. Figure 5 shows the images for two elements in sample 'q002'. Figure 5(a) shows the distribution of ^{6}Li across the quartz sample and interface. The bright area on the left-hand side of the figure is probably left-over β-eucryptite. The distribution of ^{6}Li across the quartz is almost constant and higher than the concentration of ^{7}Li (figure 5(b)).
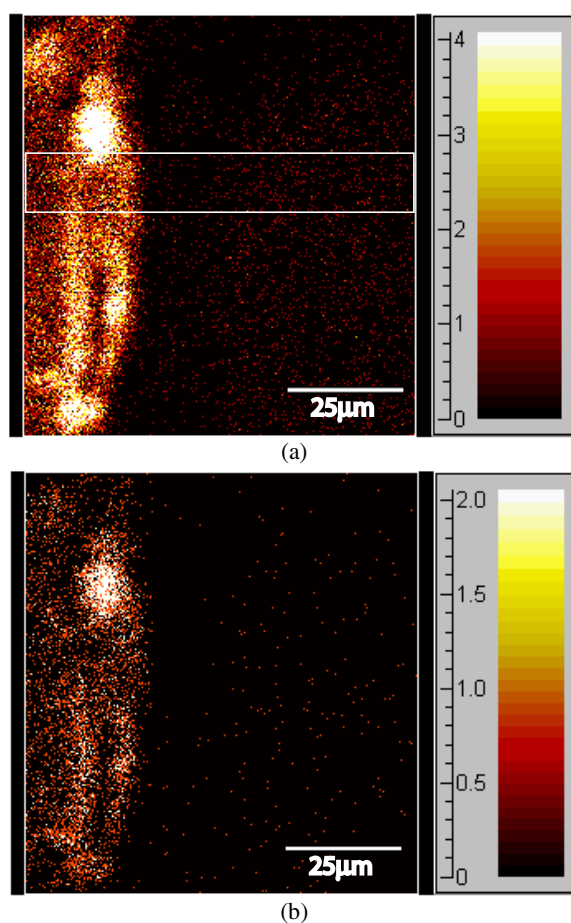
(a)

(b)

Figure 5. Images of elemental distribution taken from sample 'q002' near the doping edge. The interface is on the left-hand side. (a) ^{6}Li, (b) ^{7}Li. Lighter colours represent higher concentration. This area of the sample was chosen deliberately due to having an interface at the edge of the quartz crystal.

Table 1. Spot analysis data for four samples. All values in ppm relative to Si.

	^{6}Li (ppm)	^{7}Li (ppm)	^{27}Al (ppm)
500 edge	1.402(2)	0.188(4)	24.47(4)
500 middle	1.286(2)	0.172(4)	23.82(4)
574	2.985(1)	1.235(4)	63.15(3)
610	0.821(4)	0.559(7)	17.68(4)
q002 edge	2.137(2)	1.969(4)	61.49(3)
q002 middle	2.372(2)	2.129(2)	58.01(3)

2.5. Discussion of experimental results

As can be seen from the SIMS data on doped quartz, there are clearly two processes of ionic diffusion. First, there is 'fast Li' diffusion. This process is present in all four samples. Here Li$^+$ ions penetrate the quartz crystal and travel freely through the crystallographic channels

Table 2. Potential parameters of van Beest *et al* (1991). Partial charges: Si +2.4, O −1.2. From [17].

Interaction	A_{ij} (eV)	ρ_{ij} (Å^{-1})	C_{ij} (eV Å^{-6})
O–O	1 388.773	0.3623	175.0
Si–O	18 003.75	0.2052	133.538

perpendicular to the *c*-axis. This is confirmed by the presence of ^{6}Li across the whole of the crystals. The ratio of ^{6}Li to ^{7}Li increases with temperature (figure 4). The second process, Al + Li coupled diffusion, occurs only at the phase transition. Al ions penetrate only a short distance ($\simeq 5$ μm) into the quartz. We have seen this happening only in samples '574' and 'q002', both of which were doped at the α–β phase transition. It appears that not only Li$^+$ ions are diffusing into quartz, but also Al^{3+}. Dielectric studies on the doped samples [12] indicate Al substitutional defects in quartz, giving an increased activation energy for Li motion.

The transport data clearly exemplify the Hedvall effect [4, 5] and show the characteristic 'global hysteresis' of quartz. We attribute the transient increase of ionic current at the phase transition to the short-range penetration of Al with Li into the quartz. There is no indication that the incommensurate phase affects the long-range 'fast Li' motion; the point is discussed further in the computational part of this paper. The incommensurate phase may be connected to the Al motion, which only occurs at the phase transition.

3. Simulations

Simulations of quartz using Reverse Monte Carlo modelling fitted to total neutron scattering data [8, 14] indicate that the quartz framework is highly flexible; in the β phase, polyhedra are capable of rotating by up to 0.5 rad (26°) relative to the equilibrium position as a result of thermal motion. This corresponds to oxygen motions on the order of half an ångström. This remarkable degree of variation is achieved by collective motion of the polyhedral framework through 'rigid unit modes' (RUMs), modes of low frequency in which the polyhedra rotate with little distortion. The channel width, as represented by the distance between opposing oxygen atoms, is therefore not a static quantity but a dynamically varying one.

The flexibility of the quartz structure has been investigated by Sartbaeva *et al* [12] using the framework simulation code GASP [14] for optimizations and using GULP [15] to calculate energies using the Si–O potentials of van Beest *et al* [17] as shown in table 2. The simulation cell was a supercell of the quartz structure (β or α) containing 576 atoms (192 polyhedra). Two selected opposing oxygen atoms in the central channel of the supercell were constrained at a series of different fixed distances relative to each other, representing both contraction and expansion of the channel width. Figure 6 shows the variation of cell energy with channel width for both α and β quartz.

The flexibility of the quartz structure is reflected in the low energy cost for even quite large variations of the channel width; the opposing oxygens can be moved by $\simeq 0.5$ Å in either direction at a cost of no more than $\simeq 0.5$ eV. An animation of the framework response to these variations is available as electronic supplementary material. Large variations in channel width are therefore possible due to thermal motion of the framework.

The relative probability of observing different channel widths can be estimated by evaluating an Arrhenius factor of $\exp \frac{\Delta E}{kT}$ for each width. Figure 4 of [12] shows the probability distribution of different channel widths at 700 K (for the α-quartz structure) and 900 K (for the β structure). At 700 K the mean is 3.61 Å and the full width at half maximum (FWHM) is
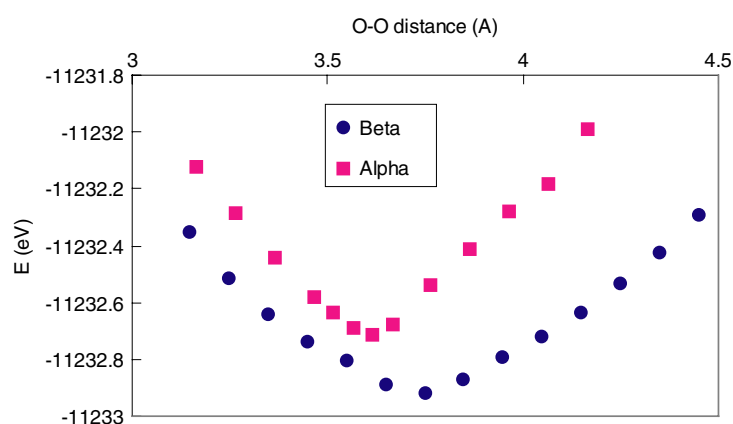
Figure 6. Cell energies as a function of O–O cross-channel distance for α-quartz and β-quartz. The energies for α-quartz have been lowered by 8 eV for easier comparison. Note the wide variation of channel width at low energy cost.

0.122 Å, while at 900 K the mean is 3.73 Å and the FWHM is 0.258 Å. These large FWHM values will be relevant to the discussion of channel shapes in the quartz (100) twin domain wall.

3.1. Minimal simulation of quartz domain wall: the effect of shear

The conventional picture of a Dauphiné-type domain wall in quartz resembles that produced by Heine's 'exaggerated gradient ploy' [18], in which a single highly elliptical channel is formed by a shear of one α domain relative to the other. Such a wall is observed at 10 K in the MD simulations of Calleja *et al* [3]. In the absence of a shear, a single line of highly distorted polyhedra would result along the domain wall, with an associated high energy cost. This, however, is true only if the polyhedra are not permitted to relax, and given the high flexibility of the quartz structure, noted above (section 3), it seems likely that the distortion can be accommodated by adjustments among the surrounding polyhedra.

We have therefore formed a minimal model of the quartz domain wall by juxtaposing two small supercells of α-quartz with opposite orientations. The simulation box for this model has parameters $a = 29.46$ Å, $b = 39.28$ Å and $c = 21.61$ Å, with $\gamma = 120°$, and contains 1728 atoms (576 polyhedra). The domain walls run along the lines of fractional coordinate $y = 0$ and 0.5. A variable degree of shear f was imposed by altering the x fractional coordinate of all atoms by $\pm f$, with domain 1 (between $y = 0$ and 0.5) and domain 2 being shifted in opposite directions. An initial series of configurations were created with different degrees of shear f and their energies were calculated in GULP. The variation of cell energy with degree of shear is shown in figure 7.

The effect of the distorted polyhedra in raising the cell energy is clear. The optimum shear was found at $f = 0.02$, corresponding to displacement of the domains by ± 0.59 Å. The difference in energy between the unsheared and optimally sheared configurations was 79.59 eV. We then relaxed the structures in GASP at both zero shear and optimum shear ($f = 0$ and 0.02), and the resulting energies (from single-point GULP calculation) are also given in figure 7. The shear was maintained throughout by pinning the lines of atoms at $y = 0.25$ and 0.75. The effect of relaxation is dramatic, reducing the energy difference between the two configurations to only 3.19 eV. This corresponds to a domain wall energy difference of only 0.04 J m^{-2}.
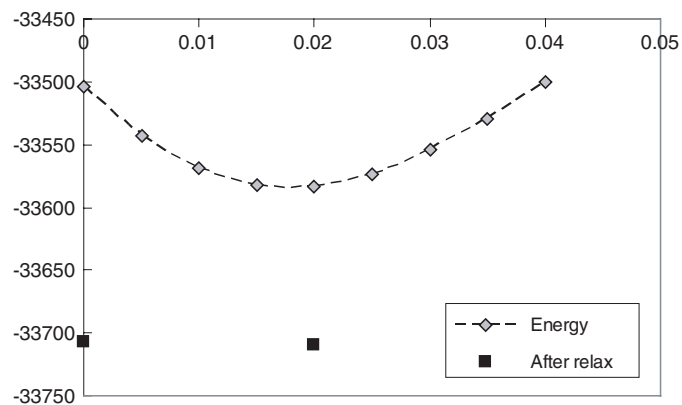
Figure 7. Energies of domain wall models, with and without relaxation of the polyhedra, versus degree of lateral shear.
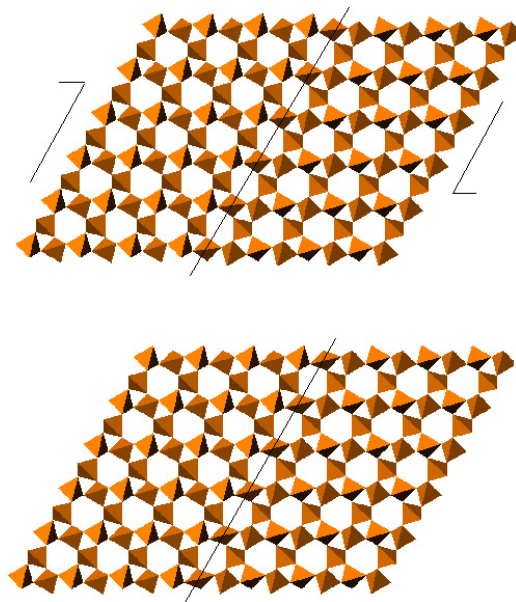

Figure 8. Minimal models of quartz domain wall, without relaxation of polyhedra. With optimal shear (above), the polyhedra at the wall are relatively little distorted. In the absence of shear (below), a single line of highly distorted polyhedra results. The domain wall is marked across the middle of the figure.

Clearly, once the polyhedra are allowed to relax, the single line of distorted polyhedra does not persist. The structures obtained without relaxation are shown in figure 8 and those with relaxation are shown in figure 9.

While these results are only approximate, given the small size of the simulation cell, they do indicate that the energy cost associated with variations in the degree of shear between the domains is far smaller than expected from the 'exaggerated gradient ploy'. This suggests that the modulation of the order parameter which gives rise to the fine microstructure of domain walls near T_c need not be accompanied by a modulation of shear between one domain and
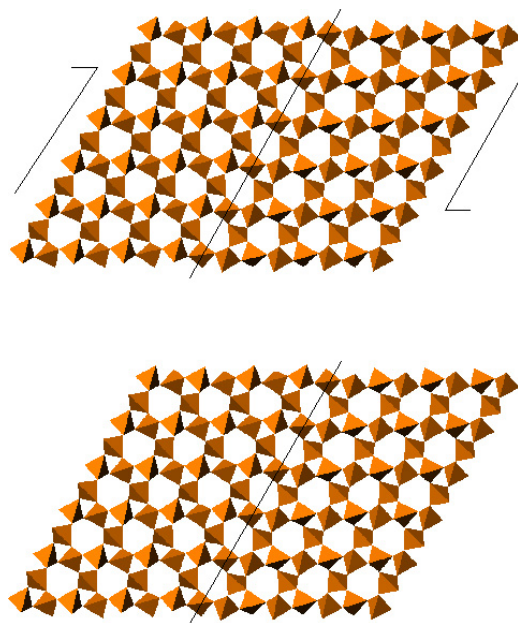
Figure 9. Minimal models of quartz domain wall, with relaxation of polyhedra. The sheared (above) and unsheared (below) configurations now resemble each other. The domain wall is marked across the middle of the figure.

another, as the highly mobile structure at high temperatures will be able to accommodate the variation in the order parameter without producing a line of highly distorted polyhedra.

3.2. Simulation of domain walls in the α and INC phases

With this in mind we have formed two simulation cells representing the (100) domain wall in quartz. The cells are greatly extended in the y-direction so as to produce a wide separation of the domain walls. The first cell is intended to represent a Dauphiné twin wall in $α$-quartz at low temperature. This cell contains two domains of $α$-quartz of opposing orientations and has dimensions $a = 29.46$ Å, $b = 117.84$ Å and $c = 21.61$ Å, with $γ = 120°$, and contains 5184 atoms (1728 polyhedra). The second cell has its lattice parameters expanded to values appropriate to the $β$ phase of quartz, with $a = 30.06$ Å, $b = 120.24$ Å and $c = 21.88$ Å. In the first cell an initial shear was established between the two domains, while in the second no shear was established. The second cell is intended to represent the formation of domains during the $β$–INC–$α$ transition and will be labelled as the INC configuration.

Pictures of the relaxed forms of both walls are given in figure 10. We may note the following points. First, while the $α$ domains in both configurations retain the trigonal form of $α$-quartz, the degree of distortion from the hexagonal $β$ form is clearly lower in the INC configuration than the $α$ configuration; that is, the expansion of the cell parameters in the INC configuration successfully generates a smaller value of the order parameter compared to the low-temperature $α$ form. Second, both structures have a recognizable domain wall with a single line of elliptically distorted channels; however, the INC configuration has a lesser degree of distortion.

We may quantify the distortion of the channels by plotting the values of the three cross-channel oxygen–oxygen distances ($R_{1,2,3}$, where R_2 is the longest and R_3 the shortest distance).
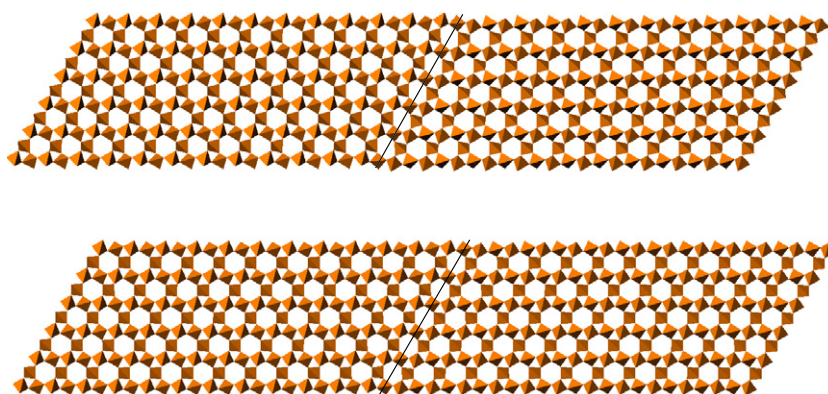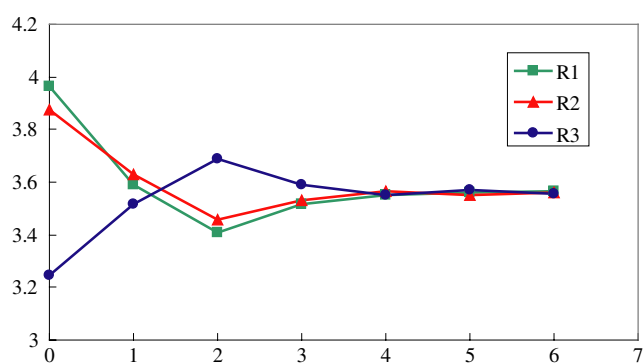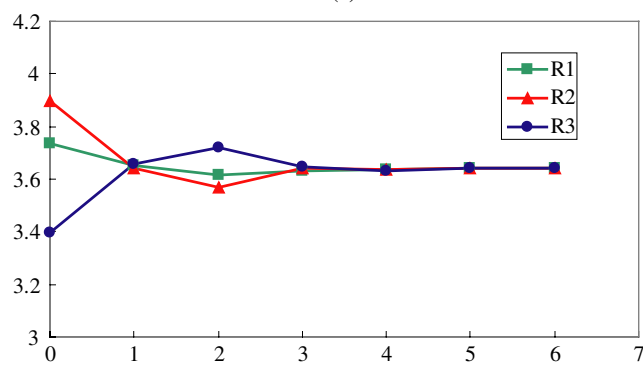
Figure 10. Models of quartz domain walls: α (above) and INC (below) configurations. Lines mark the domain walls.

(a)

(b)

Figure 11. Cross-channel oxygen–oxygen distances by channel number (0 representing the wall itself) for the (a) α and (b) INC simulation configurations. The degree of elliptical distortion is clearly lower in the INC configuration. The 'ripple' at channel 2 may be an artefact of the simulation or a real effect.

For regular α-quartz all three distances should be identical, while in the elliptically distorted channels two distances are extended and one is reduced. These values are given in figure 11 for both the wall and the neighbouring channels.
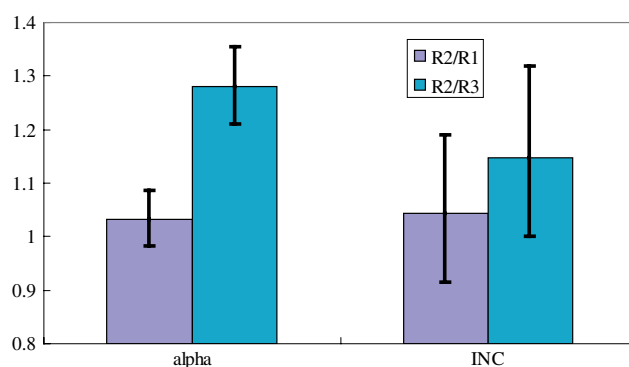
Figure 12. Ellipticities of channels in the wall; bars represent the breadth of variation, estimated from section 3. The variation in the INC structure extends to very small ellipticities, $\simeq 1$.

The values in the domain wall channel for the α form ($R_1 = 3.885$, $R_2 = 4.013$, $R_3 = 3.135$ Å) give an ellipticity $R_2{:}R_3$ of 1.28, while the values obtained by Calleja *et al* from MD simulation at 10 K ($R_2 = 4.26$, $R_3 = 3.28$ Å) [20] give an ellipticity $R_2{:}R_3$ of 1.30. The values for the INC form are ($R_1 = 3.733$, $R_2 = 3.900$, $R_3 = 3.395$ Å), showing a lower degree of elliptical distortion ($R_2{:}R_3 = 1.15$) than in the α form. This is also in line with the results of Calleja *et al* [3], for higher temperatures: 'the tetrahedral arrangement at the walls starts to resemble that in the bulk due to the markedly increased thermal disorder and the reduced size of the order parameter'.

The 'ripple' visible in channels 1–3 may be an artefact of the simulation, or a result of the 'ripples' in the order parameter predicted theoretically by Houchmanzadeh *et al* [19] and also observed in the MD simulations [3].

In the MD simulations of Calleja *et al* [3] it was found that the highly elliptical channel in the domain wall was a barrier to the motion of Na^+ ions along the [001] direction, due to the reduction of one cross-channel oxygen–oxygen distance. In order to determine whether the channels in our simulations are likely to pose a similar barrier to Li^+ motion, we should consider both the ellipticity of the channel (as represented by the ratio $R_2{:}R_3$), and the likely variation of this value due to large-amplitude thermal motion in quartz, as we calculated in section 3. Since the activation energy for Li^+ motion in quartz varies dramatically depending on the cross-channel oxygen–oxygen distance [12], the relatively short R_3 distance will only pose a serious obstacle to ionic motion if the degree of variation in that distance is so limited that it cannot reach favourable values for Li^+ motion.

In the course of the motion of the structure, the channel may become less elliptical (the long R_2 axis becoming shorter and the short R_3 axis becoming longer) or more so. We estimate the variation of ellipticity in the wall channels on the basis of the FWHM values discussed above (section 3); taking $R_2{:}R_3$ as our measure of ellipticity, the limits of likely variation are represented by $(R_2+\text{FWHM}){:}(R_3-\text{FWHM})$ at one extreme and $(R_2-\text{FWHM}){:}(R_3+\text{FWHM})$ at the other. The ratios $R_2{:}R_1$ and $R_2{:}R_3$ for the wall channels in the α and INC forms are given in figure 12, with bars representing the breadth of variation.

Clearly, in the α form, where the initial ellipticity is higher and the FWHM for variation is less, the breadth of variation is not large and the channels will always remain in more or less the same elliptical form. However, in the INC form, not only is the initial ellipticity lower, but also the degree of variation is greater; thus the variation extends to values of $R_2{:}R_3$ close to 1, that is, the channel can vary from elliptical to almost circular. The barrier to Li^+ posed by the

short R_3 distance in domain walls in the INC form should therefore be far less than the barrier posed by the low-temperature Dauphiné twin wall. On this basis, it is understandable that the phase transition does not appear to hinder the movement of Li$^+$ through the structure, despite the fine microstructure of twin walls near T_c.

In table 3 of Calleja *et al* [3], we note that the unpinning energy for Na$^+$ motion in the [001] direction along the (100) twin domain wall is considerably lower at 700 K (0.30 eV) than at 300 K (0.95 eV). Our proposal that domain walls at the phase transition in quartz do not hinder Li$^+$ motion in the same way as low-temperature domain walls is in line with this result.

4. Conclusions

The β-eucryptite–quartz system shows a dramatic example of the Hedvall effect in the transport of Al and Li into quartz. The effect is visible as a transient peak in the ionic current at the phase transition in DC transport measurements. SIMS analysis confirms that samples doped at the transition are enriched with Al and Li over a range of about 5 μm at the doping edge; this is not observed in samples doped in the α or β phases. Dielectric studies on the doped samples [12] show a process attributable to Li$^+$ motion in the presence of Al substitutional defects in quartz.

There is no evidence that the incommensurate microstructure in quartz slows lithium transport. SIMS analysis shows that the ratio of doped ^{6}Li to background ^{7}Li increases with temperature and is not reduced in the sample doped at the transition.

The use of fast framework simulation methods allows the rapid generation of very large quartz configurations for investigation of the domain wall structure. Simulations indicate that there is a low energy cost for varying the degree of shear at a (100) twin boundary in quartz; and that, while Dauphiné twin walls at low temperatures will hinder ionic transport [3], twin walls in the incommensurate phase have less elliptically distorted channels and therefore do not affect transport in the same way.

References

[1] Aird A and Salje E K H 1998 Sheet superconductivity in twin walls: experimental evidence of WO$_{3-x}$ *J. Phys.: Condens. Matter* **10** L377–80
[2] Aird A and Salje E K H 2000 Enhanced reactivity of domain walls in WO$_3$ with sodium *Eur. Phys. J.* B **15** 205–10
[3] Calleja M, Dove M T and Salje E K H 2001 Anisotropic diffusion in twinned quartz: the effect of twin boundaries *J. Phys.: Condens. Matter* **13** 9445–54
[4] Hedvall J A 1938 *Reaktionsfahigkeit fester Stoffe* (Leipzig: Johann Ambroisius Barth)
[5] Hedvall J A 1966 *Solid State Chemistry: Whence, Where and Whither* (The Netherlands: Elsevier)
[6] Dolino G 1990 The α-inc-β transitions of quartz: a century of research on displacive phase transitions *Phase Transit.* **21** 59–72
[7] Dolino G and Bastie P 2001 The role of the incommensurate phase in the opalescence of quartz *J. Phys.: Condens. Matter* **13** 11485–501
[8] Tucker M G, Keen D A and Dove M T 2001 A detailed structural characterization of quartz on heating through the α–β phase transition *Mineral Mag.* **65** 489–507

 [9] Lichtenstein A I, Jones R O, Xu H and Heaney P J 1998 Anisotropic thermal expansion in the silicate β-eucryptite: a neutron diffraction and density functional study *Phys. Status Solidi* **31** 723–37

[10] Press W, Renker B, Schulz H and Bohm H 1980 Neutron scattering of the one-dimensional ionic conductor β-eucryptite *Phys. Rev.* B **21** 1250–7

[11] Sartbaeva A, Redfern S A T and Lee W T 2004 A neutron diffraction and Rietveld analysis of cooperative Li motion in beta-eucryptite *J. Phys.: Condens. Matter* **16** 5267–78

[12] Sartbaeva A, Wells S A and Redfern S A T 2004 Li$^+$ ion motion in quartz and β-eucryptite studied by dielectric spectroscopy and atomistic simulations *J. Phys.: Condens. Matter* **16** 8173–89

[13] Gatta G D and Wells S A 2004 Rigid unit modes at high pressure: an explorative study of a fibrous zeolite-like framework with edi topology *Phys. Chem. Minerals* **31** 1–10

[14] Wells S A, Dove M T and Tucker M G 2004 Reverse Monte Carlo with geometric analysis—RMC + GA *J. Appl. Crystallogr.* **37** 536–44

[15] Gale J D and Rohl A L 2003 The General Utility Lattice Program (GULP) *Mol. Simul.* **29** 291–341

[16] Sartbaeva A 2004 Ionic transport in quartz structures *PhD Thesis* Cambridge University, Cambridge, UK

[17] Kramer G J, Farragher N P, van Beest B W H and van Santen R A 1991 Interatomic force fields for silicas, aluminophosphates, and zeolites: derivation based on *ab initio* calculations *Phys. Rev.* B **43** 506

[18] Heine V and McConnell J D C 1984 The origin of incommensurate structures in insulators *J. Phys. C: Solid State Phys.* **17** 1199–220

[19] Houchmanzadeh B, Lajzerowicz J and Salje E 1992 Interfaces and ripple states in ferroelastic crystals—a simple model *Phase Transit.* **38** 77

[20] Dr Calleja 2003 personal communication